Nanosecond resolution photography system for laser-induced cavitation based on PIV dual-head laser and industrial camera

Dixi Han [a], Rui Yuan [a], Xinkuan Jiang [a], Siyuan Geng [a], Qiang Zhong [a,b,*], Yifan Zhang [a], Zhifeng Yao [a,b], Fujun Wang [a,b]

[a] College of Water Resources and Civil Engineering, China Agricultural University, Beijing 100083, China
[b] Beijing Engineering Research Center of Safety and Energy Saving Technology for Water Supply Network System, China Agricultural University, Beijing 100083, China

ARTICLE INFO

ABSTRACT

The detailed study of the initial and collapse processes of the laser-induced cavitation requires nanosecond resolution (both nanoseconds exposure and nanoseconds interframe time) of the photography measurement system. The high-speed video cameras are difficult to achieve nanoseconds interval time. The framing and streak cameras are able to reach the nanosecond resolution, but their complex technology and expensive prices make them far from being commercially available. The present study builds a nanosecond resolution photography system based on PIV dual-head laser and conventional industrial camera. The exposure time of the photography system is controlled by the laser pulse width, which is 5 ns. The two heads of the PIV laser are operated independently thus the smallest time interval between two laser pulses can be set to less than 10 ns. A double-pulse per-exposure imaging technique is used to record the information from two laser pulses on single frame on a low-speed industrial camera. The nanosecond resolution photography system was applied to the laser-induced cavitation experiments to verify the reliability of the measurement results. The measurement of the shock wave velocity demonstrates the ability of the system to capture ultrafast phenomena, which reduces from 3611 m/s to approximately 1483 m/s within 400 ns. The experimental results also reveal the asymmetric evolution of laser-induced cavitation bubbles. The major axis of the ellipsoidal bubble has twice reversals along the laser propagation and perpendicular direction from the laser-induced breakdown to the first collapse.

1. Introduction

The cavitation phenomena following a laser-induced breakdown in liquids are the classic subject in the field of cavitation dynamics [1–6]. The entire process from the laser-induced breakdown to the first collapse of the cavitation bubbles occurs in a space on the order of millimeter within a duration of the order of 100 microseconds, and the velocity of shock waves generated during the laser-induced breakdown and bubble collapse can reach several kilometers per second[7–10]. Due to these extreme conditions, the temporal resolution of photography measurement technology needs to reach the order of nanoseconds when we focus on the initial and collapse stages[11]. The nanosecond temporal resolution in the photography measurement technology contains two requirements. The first one is the exposure time of a single image has to reduce to nanoseconds to avoid image blurring (nanosecond exposure requirement). For example, the 2000 m/s shock wave takes about 1.75 ns to traverse a single pixel (3.5 μm × 3.5 μm for a typical industrial

camera) when the optical magnification is 1×. This requires a 10 ns exposure to capture sharp images of the shock wave. The second one is the time interval between two consecutive images has to reduce to less than 10 ns (nanosecond interval requirement). For example, the velocity of shock waves usually decays from 3000 to 6000 m/s to the speed of sound in water (around 1500 m/s) within several hundred nanoseconds [7,11,12]. Thus, 10 ns temporal resolution is necessary for the detailed analysis of this shock wave rapid decay process.

The high-speed video cameras are the most commonly used photography measurement equipment in the cavitation experiments currently. However, it is difficult for the high-speed video cameras to meet the nanosecond exposure and interval requirements simultaneously. Table 1 lists performance parameters of 4 typical high-speed video cameras. The highest frame rate is 1×10^7 frames per second (fps) and minimum exposure time is 50 ns. Thus, neither the nanosecond interval nor the exposure requirement can be achieved by the high-speed video cameras themselves. The nanosecond exposure

Table 1
Main performance parameters of typical high-speed video cameras.

Type	Highest frame rate	Minimum exposure time
Phantom V2512	1.00×10^6 fps@256*32 pixels	265 ns
Photron SA-X2 type 1080 K	1.08×10^6 fps@128*8 pixels	293 ns
Specialized Imaging, Kirana-7M	7.00×10^6 fps@924*768 pixels	50 ns
Shimadzu, HyperVision HPV-X2	1.00×10^7 fps@200*125 pixels	50 ns

requirement alone can usually be realized by adding an image intensifier in front of the high-speed video cameras, or by using a nanosecond pulsed illumination source. In this setting, the camera shutter speed remains the same, but the time the camera sensor can receive light (the actual exposure time for an image) is controlled by the image intensifier or nanosecond pulsed illumination source. For example, Vogel et al. [7] used the 6 ns duration light pulse from a Q-switch laser as the illumination source. Agrez et al. [13] employed adaptive laser diodes in their illumination system. Willert et al. [14], Christian et al. [15], Wilson et al. [16] and Garen et al. [8] used pulsed LED light source to obtain tens of nanoseconds exposure time. However, the nanosecond interval requirement is still difficult to achieve in these methods. In addition, the image resolution of the high-speed video cameras is generally low at millions frame rate. One can see that the maximum image resolutions for all cameras are less than one million pixels from Table 1. The low image resolution often limits the high-precision measurement of the cavitation process.

The framing camera is a device that can achieve higher temporal resolution than the high-speed video cameras. The framing cameras employ the rotating mirror or pyramidal beam splitter to divide the light onto multiple image planes or multiple locations on the same image plane. The image number for one shot is usually 2 to 32 and the typical interframe time can be reduced to below 5 ns. The Imacon 468 framing camera, of which the framing rates can reach 1.00×10^8 fps (10 ns temporal resolution), was used by Lindau and Lauterborn [17] to study the collapse and rebound process of a laser-induced cavitation bubble near a wall. Tagawa et al. [9] used the Imacon 200 framing camera (2.00×10^8 fps) to capture the asymmetry of the laser-induced underwater shock waves.

The streak camera is the fastest imaging device currently. A streak camera deflects the light over time in the direction perpendicular to a narrow slit where the light enters into the camera and the resulting image forms a streak of light. The most advanced streak camera can reach 7.00×10^{13} fps [18]. Tomita and Shima [19] used the streaking camera Imacon 790 to study the pulse pressure and the mechanism of damage pits formed when the cavitation bubble collapsed. Noack and Vogel [12] and Pecha and Gompf [11] used Hamamatsu C5680 to capture shock wave emission during the initial and collapse stage of the cavitation, respectively. Franco Docchio et al. [20] used a streak camera to record the initial state image of the plasma in the liquid under the nanosecond laser pulse.

From the above discussion, it can be seen that the framing camera and streak camera are devices that can meet the nanosecond exposure and interval requirements simultaneously. However, complex technology, extremely high requirements for the experimental skills and expensive prices make them far from being commercially available for most of the cavitation dynamics laboratories. In the present study, a nanosecond resolution photography system, which is technically easy to use and economically affordable, is developed for the laser-induced cavitation study. The photography system employs the equipment commonly used in fluid mechanics laboratories, including PIV dual-head nanosecond pulse laser and conventional industrial camera, and the double-pulse per-exposure imaging technique to meet the

nanosecond exposure and interval requirements simultaneously. The following Section 2 will introduce the principle and setup of the photography system. Section 3 applies the system to laser-induced cavitation experiments, and Section 4 gives discussions on the results and summarizes the main conclusions.

2. Nanosecond resolution photography system

2.1. Principle

The shutter speed and interframe time of the conventional industrial camera can hardly reach the order of nanosecond simultaneously. Thus, a PIV dual-head nanosecond pulse laser is employed as the light source in the system. For the nanosecond exposure requirement, when the ambient light is blocked around the system, the industrial camera sensor can only receive light from the PIV dual-head nanosecond pulse laser. Hence, the exposure time of the image equals to the laser pulse width and it is reduced to 5 ns. For the nanosecond interval requirement, the two heads of the PIV laser can be operated independently and the minimum pulse interval can be the pulse width. The double-pulse per-exposure imaging technique is used to record images on the low-speed industrial camera. The working time of the laser and the camera is set carefully so that the two laser pulses fall within the exposure duration of a single frame of the camera.

2.2. Setup

Fig. 1 shows a sketch of the nanosecond resolution photography system. Table 2 lists the models and main parameters of equipment in the system. The New Wave Research Solo 200XT is used as the illuminating laser. This dual-head nanosecond pulse laser is part of a TSI stereo PIV system, and each head of it can emit 532 nm laser pulses within 5 ns (full width half maximum). The time interval between two pulses from two independent heads can be as small as 10 ns. The highest pulse pair repetition rate is 15 Hz. A laser beam expander is used to expand the illumination range and sulfuric acid paper and foam board are used to homogenize the laser light. A 4096 × 3000 pixels industrial camera is employed to record the images. The illuminating laser and industrial camera are arranged according to the light path of the shadowgraph photography. A macro lens (WP-8X65T, Work Power Comp.) with 8× magnification and 4.3 μm spatial resolution provides high-definition images of the laser induced cavitation. A narrow band filter with a center wavelength of 532 nm is placed before the macro lens to reduce the light from the plasma and protect the camera.

A single head Q-switched Nd:YAG pulsed laser with 10 ns pulse width is used as the ignition laser. The laser is focused in distilled water and induces the breakdown within a tank. The ignition laser, illuminating laser and the industrial camera are triggered by an 8-channel digital delay pulse generator (DDPG, Quantum composers 9528). The temporal resolution of the DDPG is 250 ps and the time jitters among different channels are smaller than 50 ps.

A beamsplitter is located at the outlet of the ignition laser to split 5% energy to the laser energy meter (Coherent J-25MB-LE) to measure and record the energy of each ignition laser pulse. Another beamsplitter is located behind the first one and another 5% energy is reflected to a photodetector (DET10A2, Thorlabs). Two photodetectors connected to an oscilloscope (DS2302A, RIGOL) are used to monitor and save the time of the ignition, first and second illuminating pulses for each experiment trial.

2.3. Timing control and double-pulse frame

In order to achieve nanosecond resolution, the working time sequence of the ignition laser, illuminating laser and industrial camera are controlled by the DDPG with 250 ps precision. Fig. 2 shows the timing control sequence of the photography system. The laser used in
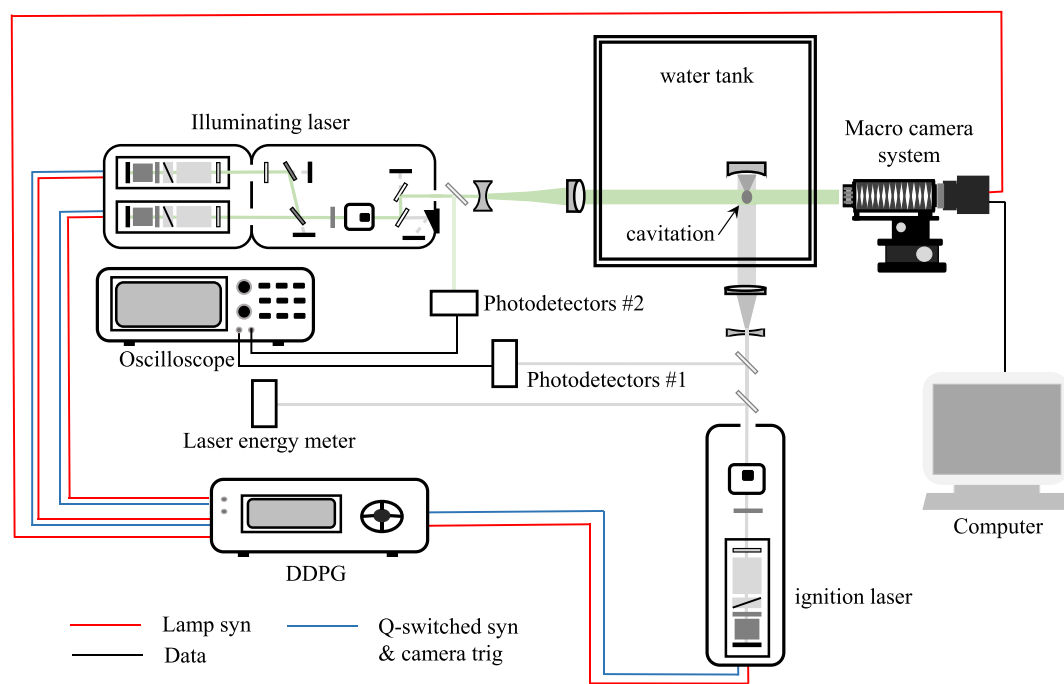
Fig. 1. Schematic diagram of the experimental system.

Table 2
Equipment used in the nanosecond resolution photography system.

Equipment	Parameter	Value	Parameter	Value
Industrial camera	Model	Daheng MARS-1230-23U3M,	Sensor model	1.1″, Global Shutter Sony IMX304 CMOS
	Image resolution	4096 × 3000 pixels	Pixel size	3.45 μm × 3.45 μm
	Frame rate	23.4fps	Shutter speed	28 μs ∼ 1 s
Ignition laser	Model	ZKLaser Plite-200	Pulse repetition rate	10 Hz
	Wavelength	1064 nm/532 nm	Pulse energy	5 ∼ 300 mJ@1064 nm
				5 ∼ 200 mJ@532 nm
	Head number	1	Pulse width	10 ns
Illuminating laser	Model	New Wave Research Solo 200XT	Pulse repetition rate	15 Hz
	Wavelength	532 nm	Pulse energy	10 ∼ 200 mJ
	Head number	2	Pulse width	5 ns
Digital Delay Pulse Generator	Model	Quantum composers 9528	Resolution	250 ps
	Channels	8	Channel to Channel Jitter	<50 ps

this study needs two trigger channels for lamp and Q-switch, respectively. The lamp should be triggered firstly then the Q-switch is triggered to emit laser pulse. The time interval between the lamp and Q-switch is a constant determined by the characteristics of the laser, and for the ignition and illuminating lasers used in present system this value is 200 μs. When the experiment starts, the ignition laser pulse is triggered firstly to create the cavitation, then the Q-switch of 1# and 2# head of the illuminating laser is triggered after T and $T + \Delta t$ respectively. The shutter duration of the camera is set to 500 μs which is much longer than the laser pulse width and Δt. The industrial camera sensor receive light from the two-illumination pulse during the shutter opening. Thus, the single frame formed after 500 μs records the bubble and shock wave images at two instances of time related to the two illumination pulses. We call this kind of picture that receives two exposures on single frame as a double-pulse frame.

Fig. 3 shows a typical double-pulse frame from this nanosecond resolution photography system. The time delay T from the breakdown is 100 ns, and Δt is 20 ns. In Fig. 3, a dark (B1) and light (B2) bubble wall, and an inner (S1) and outer (S2) shock wave can be observed. B1 and S1 are recorded by the first illuminating laser pulse and B2 and S2 are by the second one after Δt. The gap between B1 (S1) and B2 (S2) are the bubble expansion distance (shock wave propagating distance) during Δt

at the relative direction. Hence, the bubble scale, the shock wave diameter at time T, and mean velocity of bubble expansion and shock wave propagating during Δt can be directly obtained from the double-pulse frame.

The entire process of the laser induced cavitation can be studied in detail by changing T. Fig. 4 shows the cavitation bubble expansion and shock wave emission after optical breakdown caused by 60 mJ 1064 nm laser pulses. It can be seen from Fig. 4 that the photography system captures the nonspherical bubbles and shock wave after optical breakdown, which have also been reported in the literature [7,9,10,21]. Fig. 4 (a) shows that there are significant differences in the expansion velocities at different positions of the bubble wall. The expansion velocity along the propagation direction of ignition laser (horizontal) is much greater than the velocity along the perpendicular direction (vertical) in Fig. 4(a) and (b).

Table 3 lists the main performance parameters of the nanosecond resolution photography system built in this study. The exposure time is the effective light receiving time for the camera. From Fig. 2 we can see that, although the time interval between the camera opens and closes the shutter is 500 μs, the effective time for the sensor to receive light is only the pulse width of the illumination pulse. Hence, the nanosecond exposure requirement is satisfied because the width of the illuminating
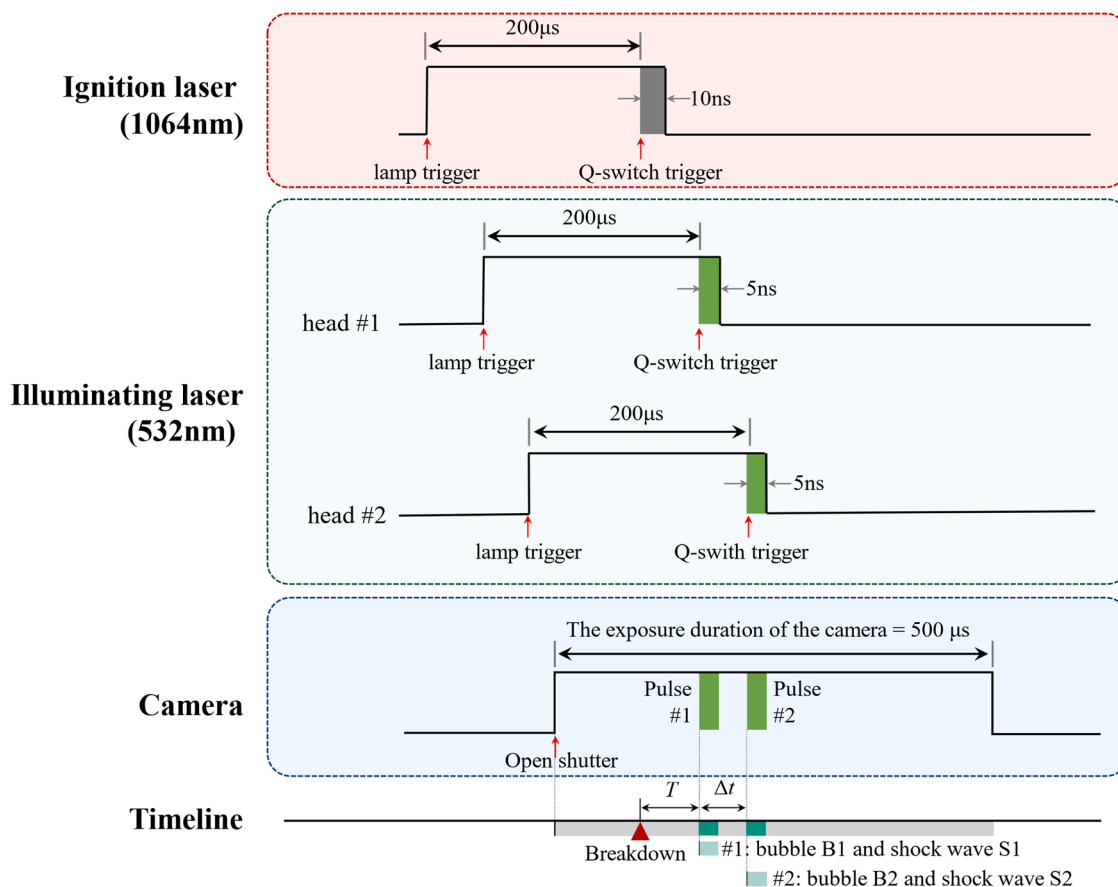
Fig. 2. Timing control relationship of the nanosecond resolution photography system.
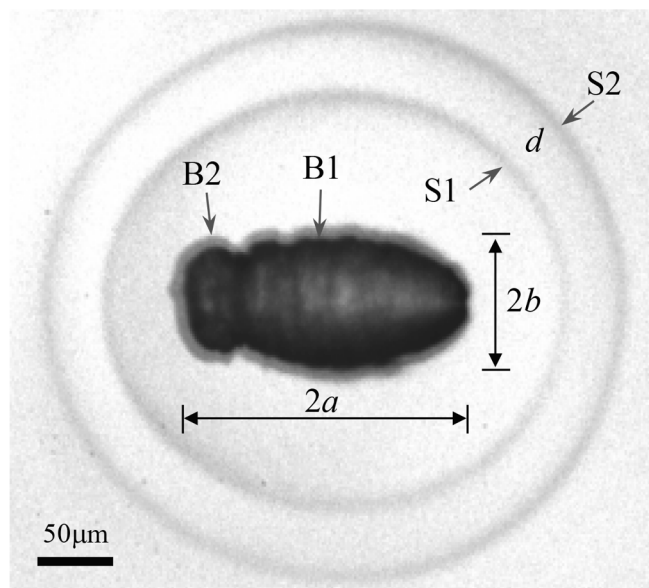

Fig. 3. A typical double-pulse frame from nanosecond resolution photography system, $T = 100$ ns and $\Delta t = 20$ ns. The first illuminating laser pulse records the bubble B1 and shock wave S1; the second illuminating laser pulse records the bubble B2 and shock wave S2. d is the distance the shock wave propagating during Δt along the marked direction. $2a$ and $2b$ are the horizontal and vertical axis of B1. The propagation direction of the laser is horizontal.

laser pulses is 5 ns. The nanosecond internal requirement depends on the scale of Δt. The minimum Δt is usually slightly bigger than the pulse width to ensure the bubbles' boundaries can be distinguished in the double-pulse frames. The smallest Δt in this study is 10 ns. Hence, the photography system meets both requirements of nanosecond resolution simultaneously.

3. Application to cavitation experiments

The nanosecond resolution photography system has 2 main advantages. The first one is that the wall speeds and scales at different positions of the bubble wall can be obtained accurately and simultaneously, so the asymmetry of the cavitation evolution can be studied in detail. This asymmetry is a remarkable feature of the laser induced cavitation. The second one is the nanosecond temporal resolution allows the system to capture extremely high-speed phenomena. This is important for the study of shock wave. In this section, the bubble evolution and shock wave propagation experiments are carried out to demonstrate the application of the nanosecond resolution photography system.

3.1. Experiment for bubble evolution

Three experimental cases for bubble evolution with different laser pulse energies are conducted. The experimental parameters for each case are listed in Table 4. It should be pointed out that due to the huge loss of laser energy in the light path and the water, the values of the laser pulse energy in Table 4 refer to the energy emitted by the laser which was calculated by the laser energy meter reading. The energy that actually inducing the optical breakdown was much smaller than the values in Table 4. The maximum radius of the cavitation bubble R_{max} and the time T_{max} to reach R_{max} are listed in Table 4 as the characteristic
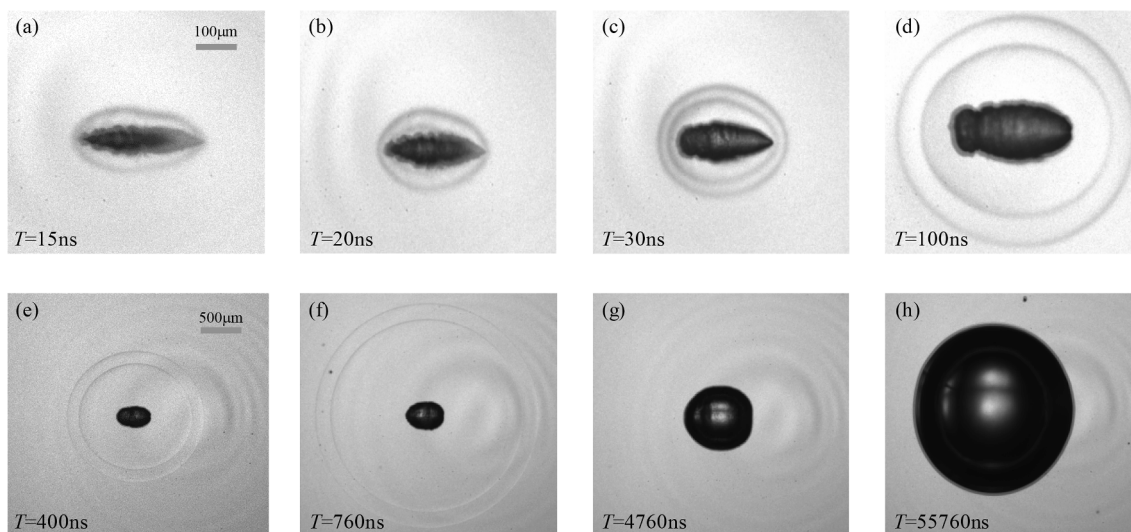
Fig. 4. Cavitation bubble expansion and shock wave emission after optical breakdown caused by 60 mJ laser pulses. The time delay of the first illuminating pulse with respect to the ignition pulse is indicated on each frame. The length scale in (a) represents a length of 100 μm for (a)-(d), and the one in (e) represents a length of 500 μm for (e)-(h).

Table 3
Main performance parameters of the nanosecond resolution photography system.

Parameter	Value
exposure time	5 ns
minimal time interval between consecutive exposures	10 ns
frames per second	10
number of exposures recorded on each frame	2
image resolution	4096 × 3000 pixels
optical magnification	8×
optical spatial resolution	4.3 μm

Table 4
Parameters for the bubble evolution experiment.

Case	Laser pulse energy (mJ)	R_{max} (μm)	T_{max} (μs)	T_{end} (μs)	Number of Samples
1	40	1282.9	120.0	237.0	50
2	80	1810.3	166.3	337.0	50
3	106	1932.1	176.0	360.0	50

scales of the cavitation. For each case, experiments with different time delay T were carried out to study the evolution of the cavitation. The measurement time covers from the optical breakdown to the time approaching the first collapse (T_{end} in Table 4). For each T, 50 independent repeated trials were carried out and all results shown later are the average value of 50 measurements. The actual T and Δt for each trial are determined from the time interval between the laser pulse peaks received by the photodetectors to avoid errors caused by the small random time drift of the lasers.

Fig. 5 shows the time evolution of the equivalent volume radius R of all cases:

$$R = \sqrt[3]{a^2 b} \qquad (1)$$

where a and b are the semi-horizontal and semi-vertical length of the bubble, respectively (see Fig. 3). T and R are dimensionless by T_{max} and R_{max}. The classic Gilmore model [4,22] for the bubble evolution is also plotted in Fig. 5. It can be seen that the dimensionless data from different cases are in good agreement with each other and the experimental data coincides well with the Gilmore model line. Since the classic Gilmore model has been repeatedly verified by a large amount of experimental

data [7], the results in Fig. 5 verify the reliability of the measurement results of present system.

Since it is impossible to focus the laser to an ideal point and the breakdown process occurs in a range with a certain length along the laser propagation direction [10], the initial stage of laser-induced cavitation is a non-spherical bubble. A main advantage of the nanosecond resolution photography system is the wall speeds and size of the bubbles along different directions can be obtained accurately and simultaneously. Fig. 6 shows the asymmetric evolution of bubbles of three cases. The upper part of Fig. 6 is the bubble wall velocity difference between horizontal (U_x) and vertical (U_y) directions. The velocity was scaled by the $U_{scale} = R_{max}/T_{max}$. The lower part of Fig. 6 is semi axis length difference of the bubble. The middle part of Fig. 6 is the carton to show the shape of the bubble in the corresponding time period.

Fig. 6 reveals that there are twice major axis reversals from the optical breakdown to the first collapse of the bubble. After the optical breakdown, the major axis of the bubbles is horizontal along the direction of the laser propagation. During $1 \times 10^{-3} < T/T_{max} < 1.45$, the bubble wall velocity along horizontal axis is smaller than that along vertical axis (U_x-$U_y < 0$). Hence, the horizontal ellipsoidal bubble gradually tends to the standard spherical shape (at approximately $T/T_{max} = 0.18$, marked as C in Fig. 6) and then evolved into a vertical ellipsoidal shape. When the bubble reaches its maximum volume (point D in Fig. 6), one can find $(a-b)/R_{max} < -0.1$ and it becomes a vertical ellipsoid. During the contraction stage, the contraction velocity of the bubble wall in the vertical direction is also faster than that in the horizontal direction. The vertical ellipsoidal bubble gradually tends to the standard spherical shape (at approximately $T/T_{max} = 1.92$, marked as E in Fig. 6) and then evolved into a horizontal ellipsoidal shape again. The grey background in the Fig. 6 marks the vertical ellipsoidal stage and the white background marks the horizontal ellipsoidal stage. Some literature has discussed non-spherical evolution of the laser induced cavitation. For example, Lim et al [21] discussed the once major axis reversal. However, the twice major axis reversals observed in Fig. 6 has not been reported to the best of the authors knowledge.

3.2. Experiment for shock wave

Three experimental cases for the shock wave induced by the optical breakdown (45, 60 and 80 mJ) are conducted to verify the ability of the photography system to measure the extremely high-speed phenomena. Since the shock wave propagating velocity is determined by the pressure
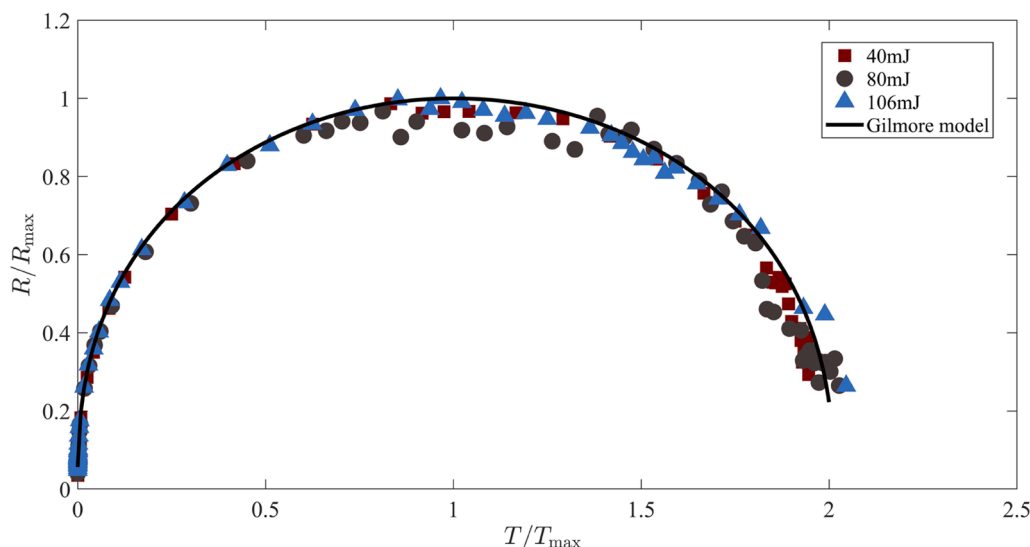
Fig. 5. Time evolution of the equivalent circle radius R of the bubble. The black line is the Gilmore model.
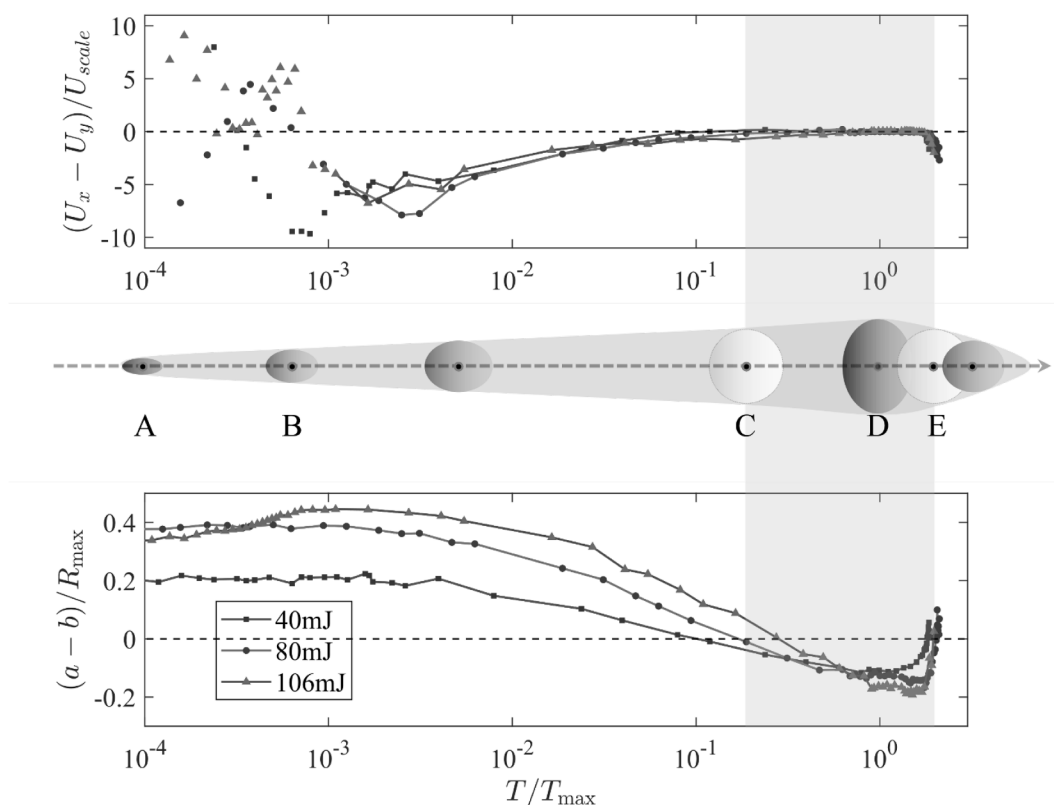

Fig. 6. Time evolution of the cavitation bubble shape. Five particular time point are marked. A marks the observation point closest to the optical breakdown; B marks the time instant when $U_x < U_y$ first appeared; C marks the time instant when the bubble first becomes a spherical shape; D marks the time instant when bubble reaches its maximum volume; E marks the time instant when the cavitation bubble becomes a spherical shape for the second time.

of the shock wave front which is closely related to the damage of the material [23], the shock wave propagating velocity is the most important parameter and can be precisely obtained by measuring the distance between two shock waves in the double-pulse frames. For each case, the measurement time lasts from the optical breakdown to 2000 ns. At $T = 2000$ ns the shock wave velocity has decayed to the speed of sound in water (1483 m/s in present experiments). The 50 independent repeated trials were carried out at each measurement instant T and all results shown later are the average value of 50 measurements.

Fig. 7 shows the evolution of the average shock wave velocity V in all directions as a function of the time delay T for all cases. The horizontal black dashed line in Fig. 7 is the speed of sound in water (1483 m/s). As shown in Fig. 7, the initial shock wave velocity is as high as several kilometers per second. The highest measured velocity for 45, 60 and 80 mJ cases are 3433 m/s. 3611 m/s and 3586 m/s, respectively. The shock wave quickly decays to the speed of sound in the water within a few hundred nanoseconds. According to the characteristics of velocity and pressure attenuation, the shock wave velocity change process can be
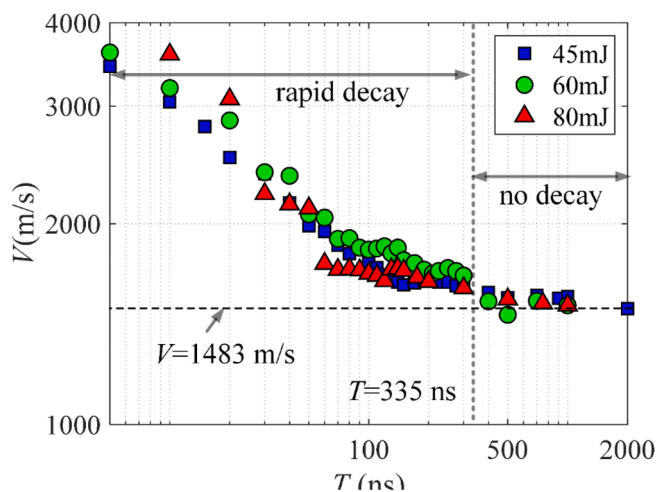
Fig. 7. Time evolution of the shock wave velocity. The horizontal dashed line is the sound speed in water 1483 m/s. The vertical dashed line is the dividing time for the rapid decay and non-decay region for 80 mJ case.

divided into two regions [17]: rapid decay region and non-decay region. Fig. 8 marks the dividing line $T = 335$ ns for 80 mJ case. After $T = 335$ ns, the shock wave keeps the speed of sound propagating in the water. For 45 mJ and 60 mJ, this dividing time are 250 ns and 310 ns, respectively. The shock wave decay process shown in Fig. 7 is consistent with the results of framing and streak cameras [12].

4. Discussion and conclusion

4.1. System scalability and application conditions

It should be noted that the successive pulse number can be recorded by the nanosecond resolution photography system in present study is 2. This is mainly limited by the number of independent heads of the illumination laser. The repetition frequency of the illumination pulse pair is 15 Hz from Table 2, Obviously the bubble recorded in the previous frame has already collapsed when the next frame is taken after 1/15 s. Hence, the present nanosecond resolution photography system essentially only records two successive instants for each bubble, which is similar to a 2-image framing camera. To increase the number of successive pulses, one can add the illuminating lasers in the system. For example, when we add another dual-head nanosecond pulse laser as the illuminating light source and combine the beams of the two illumination lasers through the optical path, we can record four successive instants on one frame as shown in Fig. 8. From Fig. 8, a DDPG with at least 11 independent output channels is needed for this 4-head illuminating lasers system. The illuminating lases cannot be increased without limit. The maximum number of successive pulses subjects to two restrictions. The first one is the laser-induced damage threshold (LIDT) of the lens used in the laser beam combining optical path. When the number of lasers increases, the laser beam expander will withstand increasing laser energy to exceed the LIDT. Assuming that the laser beam diameter before laser beam expander is 8 mm and the pulse energy is 100 mJ, the laser energy density of a single pulse is 0.2 J/cm². The typical LIDT for the laser lens is 5 J/cm². Taking into account that multiple pulses within a 10 ns interval will cause the reduction of the actual LIDT, the maximum number of laser pulses is about 12 if the actual LIDT is 2.5 J/cm². The second restriction is the discriminability of the cavitation image. The walls of different bubbles need obvious grayscale value difference to be distinguished significantly. Taking 8-bit bitmap as an example, the grayscale value varies from 0 to 255, and the effective grayscale value is usually from approximately 20 to 255 after considering the background noise. The experimental experiences show the difference in grayscale value

needs to be at least 30 to clearly distinguish different bubble walls. Thus, the maximum number of successive laser pulses per frame that can be effectively recorded is 8. In general, based on the method provided in this study one can build a nanosecond resolution photography system with similar performance parameters as an 8-image framing camera when conditions permit.

The limited number of successive images and the extremely short shooting time are the shared features of different ultra-high temporal resolution measurement systems. Hence, precise control of the time and the strictly repeatability of the event of concern are the prerequisites for the application of all ultra-high temporal resolution measurement systems. Although the method proposed in this study is a general-purpose nanosecond resolution photography, the specific system built in this study is originally designed for the laser-induced cavitation since the energy of the laser pulse and the time of optical breakdown can be precisely controlled to achieve ns-level repeatability. When one expects to apply this method to the ultrasonic cavitation, the synchronization of ultrasonic cavitation and photography system is an important consideration. The synchronization method and experiment setup in literature [24–26] in which the framing cameras were used for the ultrasonic cavitation may have some help, because the framing cameras and the nanosecond resolution photography system built in this study share the same prerequisites of precise control of the time and the strictly repeatability. In addition, the ultrasonic cavitation bubbles are usually much smaller than the laser-induced cavitation bubbles, a higher magnification lens than that used in this study have to be applied for clearly imaging. For example, de Jong et al. [24] used a microscope with 100× magnification on the framing camera for 3.5 μm ultrasonic cavitation bubbles. A larger magnification leads to a smaller field of view, which further leads to higher requirements for the repeatability of the location where the cavitation occurs.

4.2. Possible reason for major-axis reversal

The major-axis reversal of the bubble shown in Fig. 6 may be attributed to two possible mechanisms. The first mechanism is based on the mutual transformation of the kinetic energy and pressure energy of the surrounding water during the bubble evolution. After checking the velocity difference in Fig. 6, the absolute value of the vertical velocity is always greater than that of the horizontal velocity in almost all time after $T / T_{max} = 10^{-3}$. Hence, the kinetic energy of water in the vertical direction is greater than that in the horizontal direction ($E_{vy} > E_{vx}$ in Fig. 9) and the kinetic energy E_v is gradually transformed into pressure energy E_p during the expansion phase of the bubble (step 1 as shown in Fig. 9). After a period of expansion, the first reversal occurs as the instant C in Fig. 9. When the cavitation bubble expands to its maximum volume as the instant D in Fig. 9, the velocity reduces to 0, and all kinetic energy of water is converted to pressure energy. Assuming that there is no redistribution of pressure energy on the vertical and horizontal direction and the energy dissipation during the expansion process can be negligible, the pressure energy in the vertical direction is greater than that in the horizontal direction ($E_{py} > E_{px}$, $E_{vy} = E_{vx} = 0$ at D in Fig. 9). During the contraction phase (step 2 as shown in Fig. 9), the E_{vy} transformed from E_{py} is still greater than E_{vx}, thus the contraction velocity in the vertical direction is higher than that in the horizontal direction. After a period of contraction, the second major-axis reversal occurs.

The second possible mechanism is based on the difference of the surface tension. The additional pressure towards the inside of the bubble caused by the surface tension can be calculated as:

$$f = \frac{2\sigma}{r} \tag{2}$$

where σ is the surface tension coefficient, r is the radius of curvature of the bubble wall. During the expansion phase of the bubble (step 1 as shown in Fig. 9), the radius of curvature of the bubble wall on the
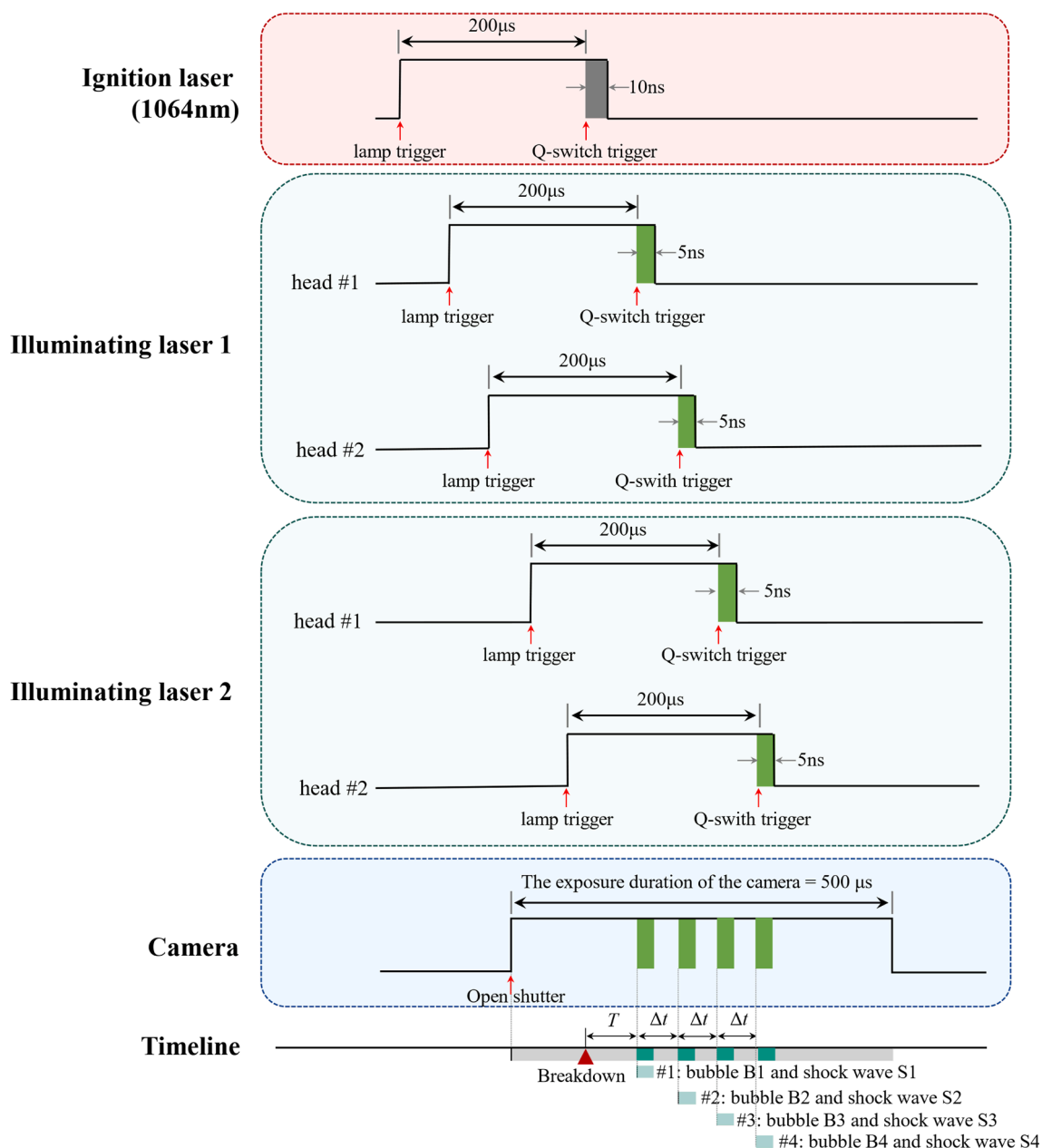
Fig. 8. Timing control relationship of the 4-head illuminating lases nanosecond resolution photography system.

horizontal axis is smaller than that on the vertical axis. The resistance to expansion in the horizontal direction is greater than that in the vertical direction (as marked by the red arrows at instant B in Fig. 9), so the expansion velocity in the horizontal direction decays faster than that in the horizontal direction. The long-term cumulative effect is that the difference between the length of the horizontal axis and the vertical axis of the bubble gradually decreases while expanding. At time instant C, the bubble changes from an ellipsoid to a spherical shape, and gradually becomes a vertical ellipsoid while it continues to expand. When the bubble reaches its maximum volume and enters the contraction phase (step 2 as shown in Fig. 9), the force to accelerate contraction in the vertical direction is greater than that in the horizontal direction (as marked by the red arrows at instant D in Fig. 9), thus the long-term cumulative effect is that the difference between the length of the horizontal and vertical axis of the bubble gradually decreases and the second major-axis reversal happens.

Regarding the primary-secondary relationship between these two

mechanisms, we currently consider that the first one may occupy a more dominant position due to the small value of the additional pressure caused by the surface tension. When the radius of the bubble is above 100 μm, the additional pressure generated by the surface tension will be less than 1451 Pa. This value is a small amount compared with other factors. However, the additional pressure caused by the surface tension always towards the inside of the bubble, the long-term cumulative effect of the surface tension may cause some observable changes. In addition, the first mechanism relies on some premise assumptions. Whether these assumptions are true in practice still needs further study. In generally, two mechanisms shown in Fig. 9 are very preliminary explanations, and since the main purpose of this study is to build an economical and technical convenient photography system with nanosecond resolution for laser-induced cavitation instead of in-depth study of the characteristics of bubbles, exploring the exact contribution of the two mechanisms to the major-axis reversal will depend on future research.
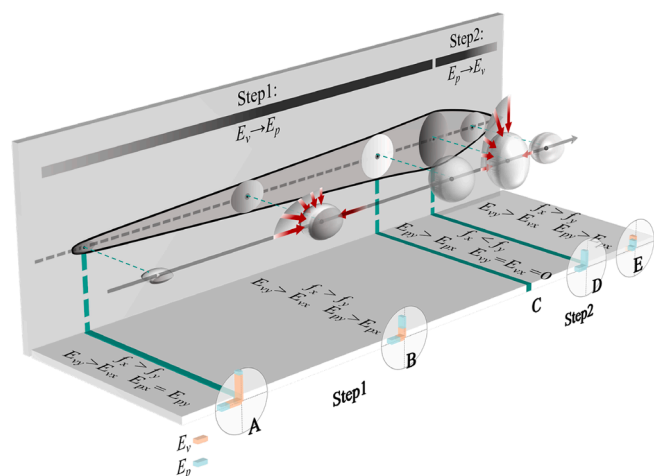
Fig. 9. Two possible mechanisms for the major-axis reversal.

4.3. Conclusion

An economical and technical convenient photography measurement system to achieve nanosecond resolution for laser-induced cavitation study is built based on the dual-head nanosecond pulse light source and double-pulse per-exposure imaging technique. Major findings are summarized as follows.

(1) A nanosecond resolution photography system was built based on a PIV dual-head nanosecond pulse laser and a regular high resolution low-speed industrial camera. The exposure time for each image is reduced to 5 ns, and the time interval between two consecutive pulses is reduced to 10 ns by operating the two laser heads independently.

(2) The double-pulse per-exposure imaging technique records the information from two exposures on a single frame. The scale of the bubble and shock wave, velocity of the bubble wall and shock wave propagation along all directions can be directly obtained from the double-pulse frames simultaneously and precisely.

(3) The nanosecond resolution photography system was applied to the laser-induced cavitation experiments. The measured bubble radius evolution process is in good agreement with the classical Gilmore model. The experimental result reveals the twice major axis reversals of the cavitation bubbles. The cavitation bubble first transforms from a horizontal ellipsoid to a vertical ellipsoid and reaches the maximum radius. Then the vertical contraction speed is faster than the horizontal contraction speed, and the bubble becomes a horizontal ellipsoid again before collapse.

(4) The nanosecond resolution photography system successfully captured the shock wave attenuation process. When the pulse energy of the ignition laser is 80 mJ, the shock wave decay from 3611 m/s to approximately 1483 m/s within 400 ns.

Data availability

The data that support the findings of this study are available from the corresponding author upon reasonable request.

Declaration of Competing Interest

The authors declare that they have no known competing financial interests or personal relationships that could have appeared to influence

the work reported in this paper.

References

[1] W. Lauterborn, Laser-induced cavitation, Acta Acust. United Acust. 31 (2) (1974) 51–78.
[2] M. Holt, Underwater explosions, Annu. Rev. Fluid Mech. 9 (1) (1977) 187–214.
[3] W. Lauterborn, C.-D. Ohl, Cavitation bubble dynamics, Ultrason. Sonochem. 4 (2) (1997) 65–75.
[4] W. Lauterborn, T. Kurz, Physics of bubble oscillations, Rep. Prog. Phys. 73 (10) (2010) 106501.
[5] C.E. Brennen, Cavitation and Bubble Dynamics, Cambridge University Press, 2014.
[6] L. Lv, Y. Zhang, Y. Zhang, Y. Zhang, Experimental investigations of the particle motions induced by a laser-generated cavitation bubble, Ultrason. Sonochem. 56 (2019) 63–76.
[7] A. Vogel, S. Busch, U. Parlitz, Shock wave emission and cavitation bubble generation by picosecond and nanosecond optical breakdown in water, J. Acoust. Soc. Am. 100 (1) (1996) 148–165.
[8] W. Garen, F. Hegedűs, Y. Kai, S. Koch, B. Meyerer, W. Neu, U. Teubner, Shock wave emission during the collapse of cavitation bubbles, Shock Waves 26 (4) (2016) 385–394.
[9] Y. Tagawa, S. Yamamoto, K. Hayasaka, M. Kameda, On pressure impulse of a laser-induced underwater shock wave, J. Fluid Mech. 808 (2016) 5–18.
[10] G. Sinibaldi, A. Occhicone, F. Alves Pereira, D. Caprini, L. Marino, F. Michelotti, C. M. Casciola, Laser induced cavitation: plasma generation and breakdown shockwave, Phys. Fluids 31 (10) (2019) 103302.
[11] R. Pecha, B. Gompf, Microimplosions: cavitation collapse and shock wave emission on a nanosecond time scale, Phys. Rev. Lett. 84 (6) (2000) 1328–1330.
[12] J. Noack, A. Vogel, Single-shot spatially resolved characterization of laser-induced shock waves in water, Appl. Opt. 37 (19) (1998) 4092–4099.
[13] V. Agrež, T. Požar, R. Petkovšek, High-speed photography of shock waves with an adaptive illumination, Opt. Lett. 45 (6) (2020) 1547–1550.
[14] C. Willert, B. Stasicki, J. Klinner, S. Moessner, Pulsed operation of high-power light emitting diodes for imaging flow velocimetry, Meas. Sci. Technol. 21 (7) (2010) 075402.
[15] C.E. Willert, D.M. Mitchell, J. Soria, An assessment of high-power light-emitting diodes for high frame rate schlieren imaging, Exp. Fluids 53 (2) (2012) 413–421.
[16] C.T. Wilson, T.L. Hall, E. Johnsen, L. Mancia, M. Rodriguez, J.E. Lundt, T. Colonius, D.L. Henann, C. Franck, Z. Xu, J.R. Sukovich, Comparative study of the dynamics of laser and acoustically generated bubbles in viscoelastic media, Phys. Rev. E 99 (4) (2019), 043103.
[17] O. Lindau, W. Lauterborn, Cinematographic observation of the collapse and rebound of a laser-produced cavitation bubble near a wall, J. Fluid Mech. 479 (2003) 327–348.
[18] P. Wang, J. Liang, L.V. Wang, Single-shot ultrafast imaging attaining 70 trillion frames per second, Nat. Commun. 11 (1) (2020) 1–9.
[19] Y. Tomita, A. Shima, Mechanisms of impulsive pressure generation and damage pit formation by bubble collapse, J. Fluid Mech. 169 (-1) (1986) 535–564.
[20] F. Docchio, P. Regondi, M.R. Capon, et al., Study of the temporal and spatial dynamics of plasmas induced in liquids by nanosecond Nd: YAG laser pulses. 1: Analysis of the plasma starting times, Appl. Opt. 27 (17) (1988) 3661–3668.
[21] K.Y. Lim, P.A. Quinto-Su, E. Klaseboer, B.C. Khoo, V. Venugopalan, C.-D. Ohl, Nonspherical laser-induced cavitation bubbles, Phys. Rev. E 81 (1) (2010), 016308.
[22] F.R. Gilmore. The growth or collapse of a spherical bubble in a viscous compressible liquid, 1952.
[23] J. Gu, C. Luo, Z. Lu, P. Ma, X. Xu, X. Ren, Bubble dynamic evolution, material strengthening and chemical effect induced by laser cavitation peening, Ultrason. Sonochem. 72 (2021) 105441.
[24] N. De Jong, P.J. Frinking, A. Bouakaz, et al. Optical imaging of contrast agent microbubbles in an ultrasound field with a 100-MHz camera[J], 2000, 26(3): 487-492.
[25] M. Postema, A. Bouakaz, C.T. Chin, et al. Optically observed microbubble coalescence and collapse[C]. 2002 IEEE Ultrasonics Symposium, 2002. Proceedings, 2002: 1949-1952.
[26] M. Postema, A. Van Wamel, F.J. Ten Cate, et al. High-speed photography during ultrasound illustrates potential therapeutic applications of microbubbles[J], 2005, 32(12): 3707-3711.